Turbulence Characteristics in an Elevated Shear Layer over Owens Valley

QINGFANG JIANG

UCAR, Monterey, California

JAMES D. DOYLE

Naval Research Laboratory, Monterey, California

VANDA GRUBIŠIĆ

Department of Meteorology and Geophysics, University of Vienna, Vienna, Austria

RONALD B. SMITH

Department of Geology and Geophysics, Yale University, New Haven, Connecticut

(Manuscript received 26 March 2009, in final form 14 February 2010)

ABSTRACT

Characteristics of turbulence in the lower and middle troposphere over Owens Valley have been examined using aircraft in situ measurements obtained from the Terrain-Induced Rotor Experiment. The two events analyzed in this study are characterized by a deep turbulent layer from the valley floor up to the midtroposphere associated with the interaction between trapped waves and an elevated shear layer. Kelvin–Helmholtz (KH) instability develops above the mountaintop level and often along the wave crests where the Richardson number is reduced. The turbulence induced by KH instability is characterized by a progressive downscale energy cascade, a well-defined inertial subrange up to 1 km, and large eddies with vertical to horizontal aspect ratios less than unity. The turbulence below the mountaintop level is largely shear induced, associated with wave steepening and breaking, and is more isotropic. Evaluation of structure functions indicates that while the turbulence energy cascade is predominately downscale, upscale energy transfer exists with horizontal scales from a few hundred meters to a few kilometers because of the transient energy dispersion of large eddies generated by KH instability and gravity wave steepening or breaking.

1. Introduction

Turbulence is ubiquitous in high Reynolds fluids such as the earth's atmosphere. Atmospheric turbulence has been the subject of numerous studies, mostly based on field observations or wind tunnel experiments. However, compared to boundary layer turbulence, detailed documentation of atmospheric turbulence in mountainous areas is still relatively rare. Complexity over mountains is enhanced in part because turbulence can be generated by mountain waves at levels well above the atmospheric boundary layer. It follows that observing turbulence over mountainous areas often requires relatively expensive platforms such as well-equipped research aircraft. Lilly and Lester (1974) examined stratospheric waves and turbulence using high-altitude aircraft in situ measurements over the Sangre de Cristo Mountains of Southern Colorado obtained from the Colorado Lee Wave Observational Program. They found that multiple peaks were present in the power spectra of velocities and potential temperature, associated with mountain waves and wave-induced turbulence. The mean slopes of these spectra were approximately -3 for scales between 3 and 20 km, likely related to breaking gravity waves. The absence of a $-5/3$ slope in the small-scale limit was attributed to observational inaccuracy. Strong turbulence was observed in the midtroposphere over central Colorado on 11 January 1972 associated with a severe downslope windstorm (Lilly 1978). The strong vertical wind shear induced by large-amplitude waves and the subsequent

Corresponding author address: Qingfang Jiang, UCAR, 7 Grace Hopper Ave., Monterey, CA 93943.
E-mail: jiang@nrlmry.navy.mil

DOI: 10.1175/2010JAS3156.1

Report Documentation Page

Form Approved
OMB No. 0704-0188

1. REPORT DATE	2. REPORT TYPE	3. DATES COVERED
JUL 2010		**00-00-2010 to 00-00-2010**

4. TITLE AND SUBTITLE	5a. CONTRACT NUMBER
Turbulence Characteristics in an Elevated Shear Layer over Owens Valley	5b. GRANT NUMBER
	5c. PROGRAM ELEMENT NUMBER
6. AUTHOR(S)	5d. PROJECT NUMBER
	5e. TASK NUMBER
	5f. WORK UNIT NUMBER
7. PERFORMING ORGANIZATION NAME(S) AND ADDRESS(ES) **UCAR,Monterey,CA**	8. PERFORMING ORGANIZATION REPORT NUMBER
9. SPONSORING/MONITORING AGENCY NAME(S) AND ADDRESS(ES)	10. SPONSOR/MONITOR'S ACRONYM(S)
	11. SPONSOR/MONITOR'S REPORT NUMBER(S)

12. DISTRIBUTION/AVAILABILITY STATEMENT
Approved for public release; distribution unlimited

13. SUPPLEMENTARY NOTES

14. ABSTRACT

Characteristics of turbulence in the lower and middle troposphere over Owens Valley have been examined using aircraft in situ measurements obtained from the Terrain-Induced Rotor Experiment. The two events analyzed in this study are characterized by a deep turbulent layer from the valley floor up to the midtroposphere associated with the interaction between trapped waves and an elevated shear layer. Kelvin?Helmholtz (KH) instability develops above the mountaintop level and often along the wave crests where the Richardson number is reduced. The turbulence induced by KH instability is characterized by a progressive downscale energy cascade, a well-defined inertial subrange up to 1 km, and large eddies with vertical to horizontal aspect ratios less than unity. The turbulence below the mountaintop level is largely shear induced, associated with wave steepening and breaking, and is more isotropic. Evaluation of structure functions indicates that while the turbulence energy cascade is predominately downscale, upscale energy transfer exists with horizontal scales from a few hundred meters to a few kilometers because of the transient energy dispersion of large eddies generated by KH instability and gravity wave steepening or breaking.

15. SUBJECT TERMS

16. SECURITY CLASSIFICATION OF:			17. LIMITATION OF ABSTRACT	18. NUMBER OF PAGES	19a. NAME OF RESPONSIBLE PERSON
a. REPORT **unclassified**	b. ABSTRACT **unclassified**	c. THIS PAGE **unclassified**	**Same as Report (SAR)**	**17**	

development of shear instability were believed to be responsible for the observed midtropospheric turbulence. Again, the $-5/3$ power law was not observed in the velocity and potential temperature spectra. Stratified turbulence associated with a bora event was examined by Mahrt and Gamage (1987), and a variety of structure functions were evaluated using the aircraft data obtained from the Alpine Experiment. They found that the observed turbulence was strongly influenced by stratification. In 1999, a midtropospheric mountain wave breaking event over the Central Alps was documented during the Mesoscale Alpine Program (Jiang and Doyle 2004). The velocity spectra derived from two available legs exhibited a $-5/3$ slope from the smallest resolvable scale up to approximately 4 km and the mean slopes were -2 or -3 for larger scales. A relatively large positive buoyancy production rate was found along one of the legs, implying wave-induced local overturning of isentropic surfaces. More recently, Doyle et al. (2005) studied a large-amplitude mountain wave event over Greenland observed during the Fronts and Atlantic Storm-Track Experiment (FASTEX). Multiple energy-containing peaks were found from the velocity spectra. These peaks were attributed to large eddies induced by breaking mountain waves. Clearly, understanding turbulence over complex terrain remains a challenging problem. In mountainous areas, turbulence could be generated by multiple mechanisms, including wave-induced shear and convective instability associated with overturning of isentropic surfaces, and, in the lower troposphere, terrain-scale circulations driven by differential heating.

The Terrain-Induced Rotor Experiment (T-REX) took place in March and April 2006 over and within Owens Valley in California. Owens Valley is a quasi-two-dimensional valley located between two nearly parallel mountains, the Sierra Nevada and the Inyo Mountains (Fig. 1). Strong mountain waves and rotors can be generated over Owens Valley as the westerly or southwesterly flow impinges on the southeast–northwest-oriented topography. The objectives of T-REX include advancing our understanding of mountain wave–induced rotors, interaction between waves and turbulence, and differential heating–forced circulations within the valley (Grubišić et al. 2008). In addition to the dense ground-based instruments deployed in Owens Valley, the University of Wyoming King-Air (UWKA) flew stacked legs in the lower and middle troposphere along a track oriented approximately across Owens Valley (Fig. 1) to sample gravity waves and turbulence during each intensive observational period (IOP). Approximately two dozen UWKA flights were conducted during the two-month-long field observational period, which provided a valuable dataset for studying waves and turbulence over complex terrain. In this study, we analyze two UWKA flights with a focus on the characteristics of turbulence over Owens Valley. In particular, we want to deepen our understanding of issues such as wave and turbulence interaction, characteristics of large eddies associated with wave-induced Kelvin–Helmholtz (KH) instability, the turbulence inertial subrange, turbulence intermittency, and cross-scale energy transfer over complex terrain.

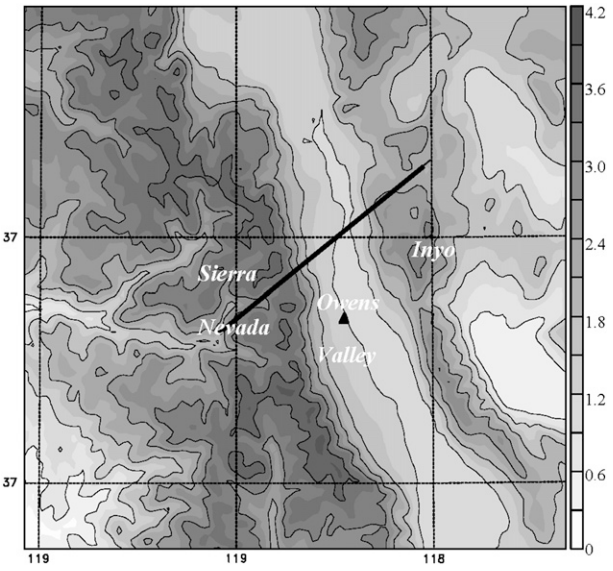

FIG. 1. The terrain height in the observational area, including Owens Valley, central Sierra Nevada, and Inyo Mountains, is shown in grayscale (interval: 0.3 km) and contours (interval: 0.6 km). The NCAR ISS site is marked by a triangle and the UWKA flight track is indicated by a bold line.

The remainder of this paper is organized as follows. The relevant observational details and flow conditions are described in section 2. General wave, eddy, and turbulence characteristics are illustrated in section 3. Breaking KH billows observed along four midtroposphere legs are examined in section 4. In section 5, the turbulence characteristics are analyzed. The in situ measurements from another IOP are examined in section 6. The results are summarized in section 7.

2. Background

a. King-Air measurements

During each westerly IOP (i.e., each IOP with prevailing westerly or southwesterly winds at the mountaintop level), the UWKA flew stacked legs along a track oriented across Owens Valley and approximately parallel to the wind direction at the mountaintop level (~4 km MSL). The altitude of flight legs ranges from 1400 m (i.e., approximately 300 m above the valley floor) to 8500 m MSL (Table 1). The leg lengths vary approximately from

TABLE 1. IOP 4a flight traverse summary. The possible ranges for upscale energy transfer are derived from third-order structure functions.

Leg	Time (UTC)	Alt (m)	Char	Data points	a	Upscale range (m)
1	1656–1702	7590	Wave	9025	0.10	—
2	1705–1721	5750	Wave	24 025	0.12	—
3	1723–1730	6660	Wave	9775	0.08	—
4	1733–1750	5470	KH	25 525	0.16	370 up
5	1751–1759	5150	KH	11 275	0.25	850–1500
6	1801–1816	4840	KH	22 525	0.25	2800–3500
7	1818–1825	4620	KH	11 525	0.42	500–1000
8	1827–1833	4240	Turb	9025	0.39	—
9	1840–1845	3930	Turb	6775	0.38	380–550
10	1846–1854	3620	Turb	11 275	0.60	490 up
11	1858–1903	3300	Turb	7025	0.69	950 up
12	1905–1909	3000	Turb	6775	—	860 up
13	1914–1918	2670	Turb	5525	—	—
14	1920–1924	2390	Turb	7025	—	—
15	1929–1932	2080	Turb	5525	—	150–400
16	1933–1936	1790	Turb	5275	—	—

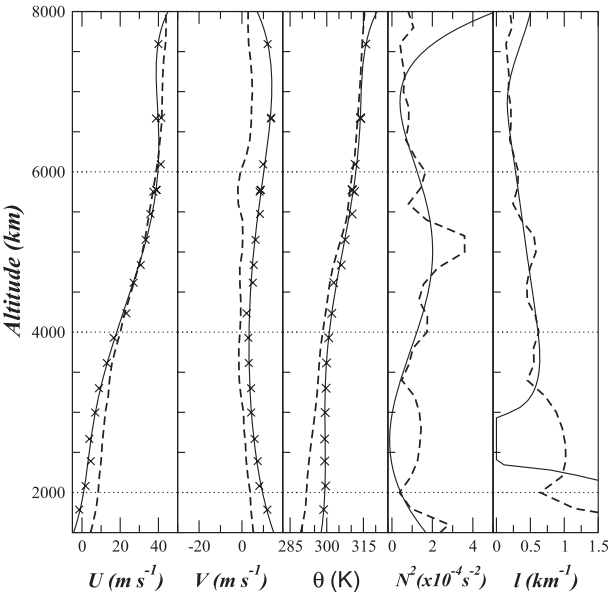

FIG. 2. Profiles of (left)–(right) U, V, θ, N^2, and l are shown. The dashed profiles are derived from the 1800 UTC 14 Mar 2006 sounding launched from the MAPR site in Owens Valley. The crosses represent data points from the means of each UWKA leg, and the solid curves correspond to sixth-order regressions of U, V, and θ using the UWKA means.

15 km (i.e., in-valley legs) to 80 km (above-mountaintop legs). The average true airspeed of UWKA is approximately 100–110 m s^{-1} for the long legs above the mountaintop and approximately 80–90 m s^{-1} for the short in-valley legs. The data frequency is 25 Hz. In addition to the UWKA data, radiosondes launched from the National Center for Atmospheric Research (NCAR) Integrated Sounding System (ISS) located at the Independence Airport are analyzed as well.

In this study, we focus on the 14 March 2006 morning flight executed during IOP 4 (referred to as IOP 4a hereafter). UWKA took off at approximately 1600 UTC [i.e., 0800 Pacific Standard Time (PST)] and returned to the Bishop airport at approximately 2000 UTC (i.e., 1200 PST). The UWKA sampled from the middle troposphere down to approximately 600 m above the valley floor over a 2.5-h period and the vertical spacing between two adjacent legs was approximately 300 m with the exception of the top two legs. In addition, we have analyzed the morning flight on 2 March during IOP 1 (hereafter referred to as IOP 1a) and the results are compared with IOP 4a in section 6. The UWKA instrumental error ranges are 0.5 K for potential temperature, 1 m s^{-1} for horizontal velocity, 0.15 m s^{-1} for vertical velocity, and 0.5 hPa for pressure.

b. Mean flow conditions

Results from the Coupled Ocean–Atmospheric Mesoscale Prediction System (COAMPS)[1] simulations with a 27-km grid increment (not shown) indicate that the large-scale flow conditions for IOPs 1a and 4a are both characterized by a pressure trough positioned off the Alaska Coast, which directs the southwesterly flow toward the Sierra Nevada and Owens Valley. During the observational periods, the prevailing winds at the mountaintop level are southwesterly and the UWKA flight tracks are oriented approximately along the mountaintop level wind direction. In the remainder of the paper, U and V denote the along-track (also referred to as longitudinal or cross-valley) and the normal (also referred to as along-valley) wind components, respectively.

Figure 2 shows profiles derived from the 1800 UTC 14 March sounding launched from the NCAR ISS near Independence; the corresponding variables averaged from each leg of the UWKA IOP 4a flight are included for comparison. The radiosonde measurements have been averaged over a vertical distance of 300 m, which is comparable to the average vertical distance between two adjacent UWKA legs. The wind and potential temperature profiles from the two different datasets agree with each other reasonably well. The discrepancies could be due to the horizontal variation of the measured fields and the time lag between the radiosonde and the UWKA flight. For example, the potential temperature measured by the UWKA at the 1790-m level near 1930 UTC is approximately 8 K warmer than that derived from the

[1] COAMPS is a registered trademark of the Naval Research Laboratory.

1800 UTC (i.e., launched near 1700 UTC) radiosonde, probably because of the warming of the low-level valley air associated with the surface heating between 1700 and 1930 UTC. The cross-valley wind profile is characterized by weak winds (<10 m s^{-1}) below 3.5 km MSL, strong winds (~40 m s^{-1}) above 5.5 km, and a shear layer located between 3.5 and 5.5 km. The along-valley wind component is southerly in the valley and is much weaker than the along-track component above the mountaintop level. A stable layer exists between 4 and 5.5 km, coincident in altitude with the shear layer above the mountaintop. The air in the valley is much less stable.

Also shown in Fig. 2 are the buoyancy frequency squared $N^2(z)$ defined by $N^2 = (g/\theta)(\partial\theta/\partial z)$, and the Scorer parameter $l(z)$ defined by $l^2 = N^2/U^2 - (1/U)(d^2U/dz^2)$, where g is the gravitational acceleration and θ is the potential temperature. It is noteworthy that N^2 computed from UWKA leg-average potential temperature is negative between 2.5 and 3 km MSL, indicative of the presence of an elevated mixed layer. A similar elevated mixed layer was observed during the Sierra Rotor Project (Jiang and Doyle 2008) associated with a shallow layer of westerly flow across the valley floor. The N^2 profiles derived from both the radiosonde measurements and UWKA leg means exhibit a maximum between 4.5 and 5.5 km. It is also interesting to note that the value of N^2 derived from the radiosonde is larger than 3×10^{-4} s^{-1} between 4.75 and 5.25 km, coincident with a vertical wind shear maximum of approximately 0.015 s^{-1}. Associated with the stability variation and the increase in U, the Scorer parameter decreases gradually with altitude in the 4–7-km layer, which may serve as a wave duct and promote the formation of trapped waves in the lee of topography (Scorer 1949).

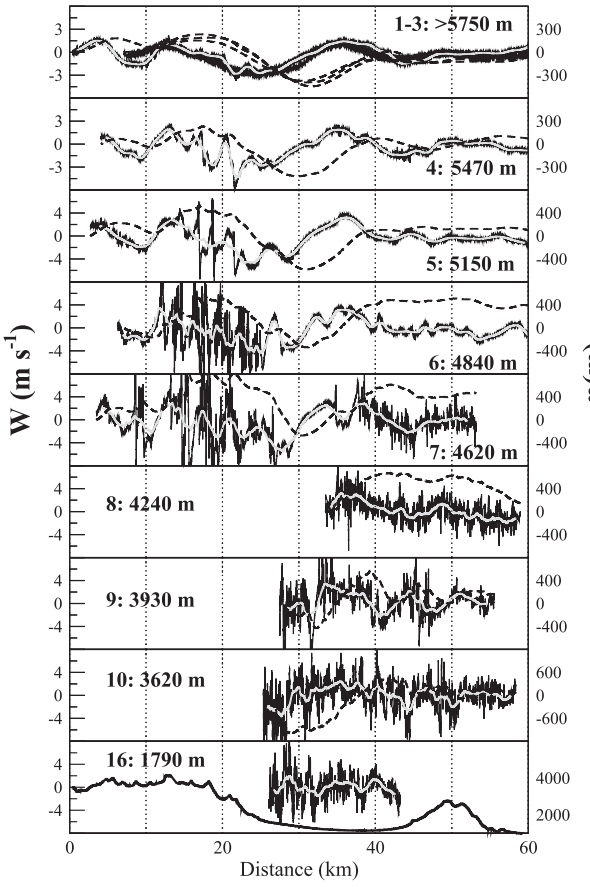

FIG. 3. The 25-Hz vertical velocity is plotted as a function of the horizontal distance from a reference point over the Sierra ridge (the west end point of the top leg) for legs (top)–(bottom) 1–10 and 16, including topography. The corresponding vertical displacement and filtered vertical velocity curves are shown as dashed and gray curves, respectively. Note the variation in ranges of w and η.

3. Waves, KH instability, and turbulence

The 25-Hz vertical velocities observed along vertically stacked legs as a function of distance from a reference point over the Sierra Ridge (i.e., the western end of the longest leg) are shown in Fig. 3. Within the vertical cross section, UWKA sampled small-scale turbulence, kilometer-scale eddies, and mountain waves with wavelengths on the scale of 20–30 km. In this study, we use the terms ''waves,'' ''large eddies,'' and ''turbulence'' to loosely refer to perturbations with scales greater than 6 km, between 500 m and 6 km, and smaller than 500 m, respectively. The choice of the eddy size range is largely based on the spectral and wavelet analysis in the following sections. For the convenience of discussion, we separate the 16 legs into three groups. The top three legs above 5.5 km, characterized by relatively smooth waves, are referred to as wave legs. The flight segments below the mountaintop are predominately turbulence and are therefore referred to as turbulence legs. The four legs between 4.5 and 5.5 km MSL are characterized by coexistence of smooth waves, large eddies, and high-frequency turbulence. We refer to these legs as KH legs based on the discussion presented later in the paper.

a. Trapped waves

Also included in Fig. 3 are the vertical velocity smoothed with a 250-point (i.e., ~1 km) running mean filter for each leg, and the vertical displacement for the top 10 legs. The vertical displacement $\eta(x)$ is derived using the steady-state linear relation (Smith et al. 2008)

$$\eta(x) = \int_0^x (w/U)\, dx, \tag{1}$$

where w is the vertical velocity, U is based on a five-point average, and $\eta(x)$ is computed only for legs with the minimum U greater than 3 m s^{-1}. Note that the curves

for the three wave legs above 5.5 km shown in the top panel agree with each other well.

Regardless of the time lag between these legs, vertically coherent wave patterns are evident for the wave, KH, and top turbulence legs near the mountaintop level, indicating that the waves are relatively steady over the approximately 2.5-h observational period and penetrate into the valley. At least two wave crests are evident from the wave and KH legs with a wavelength of approximately 25 km (Fig. 3). The first wave crest is located over the lee slope of the Sierra ridge and the second, with a much reduced amplitude, is located over the eastern portion of the valley. The observed wave crests and troughs are vertically aligned (Fig. 3), suggesting that these waves are probably trapped waves. As demonstrated in Smith et al. (2008), a useful parameter for diagnosing trapped waves from aircraft data is the wave energy equipartition ratio (EQR); EQR = $\overline{\mathrm{PE}}/\overline{\mathrm{KE}}$, where $\overline{\mathrm{PE}} = -(\overline{\rho}g/2\overline{T})\overline{\theta'\eta'}$ and $\overline{\mathrm{KE}} = (\overline{\rho}/2)(\overline{u'^2 + v'^2 + w'^2})$ are the transect-averaged potential and kinetic energy, ρ and T are the air density and temperature, respectively, the overbars denote transect means, and the primed variables represent perturbations relative to their leg means. For a pure propagating wave, the wave EQR should be unity and any departure from unity indicates the presence of both up- and downgoing waves (Smith et al. 2008). The EQR values estimated from the top three legs are 0.067, 0.11, and 0.48, respectively, further substantiating that the observed waves are indeed trapped. The decay of trapped waves downstream could be caused by boundary layer absorption (Jiang et al. 2006) or wave energy leaking aloft.

b. KH instability

According to linear theory, KH instability may occur in stably stratified shear flow when the gradient Richardson is less than ¼ (Miles 1961; Howard 1961). The development of KH instability usually leads to the formation of a series of parallel roll vortices (often referred to as KH waves, KH billows, or KH eddies) oriented along the wind direction. KH instability has been the subject of numerous theoretical, experimental (e.g., Thorpe 1968), and numerical (e.g., Klaassen and Peltier 1985; Fritts et al. 1996) studies. KH eddies can be made visible by clouds (i.e., billow clouds) or can be observed by Doppler radars in the optically clear atmosphere. However, direct observations of KH eddies by research aircraft are still rare.

Legs 4–7 are located between 4.5 and 5.5 km, a layer characterized by strong vertical wind shear (i.e., mean shear $\sim 0.013\ \mathrm{s}^{-1}$) and relatively large static stability ($N^2 > 2 \times 10^{-4}\ \mathrm{s}^{-2}$; Fig. 2). We estimate the gradient Richardson number Ri, defined as $\mathrm{Ri} = N^2(\overline{U}_z^2 + \overline{V}_z^2)^{-1}$, using sixth-order polynomial regressions of the transect means, (i.e., $\overline{U}$, $\overline{V}$, and $\overline{\theta}$) to obtain the vertical derivatives

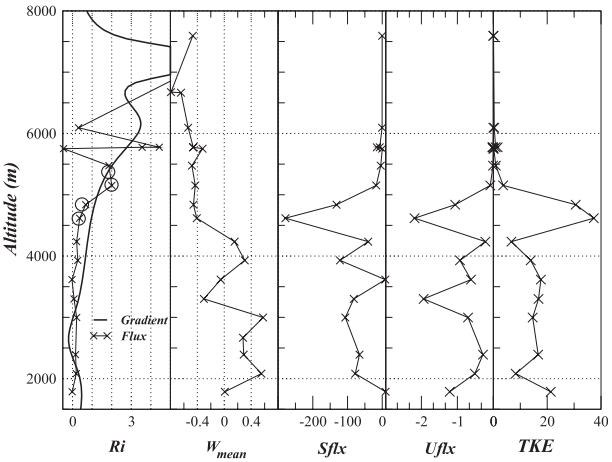

FIG. 4. Profiles of (left)–(right) gradient and flux Richardson numbers, leg-averaged vertical velocity (m s^{-1}), sensible heat flux (W m^{-2}), vertical flux of the cross-valley momentum component (N m^{-2}), and TKE ($\mathrm{m}^2\ \mathrm{s}^{-2}$) for each leg.

of those variables (Fig. 4). In addition, the flux Richardson number $\mathrm{Ri}_f = b/s$, where $b = (g/\overline{\theta})\overline{\theta''w''}$ is the buoyancy production rate of turbulent kinetic energy (TKE) and $s = \overline{u''w''}(\partial\overline{U}/\partial z) + \overline{v''w''}(\partial\overline{V}/\partial z)$ is the shear production rate, estimated from all flight legs is included in Fig. 4 as well. The double-primed variables denote perturbations associated with large eddies and turbulence, obtained by subtracting the 6-km moving averages to remove mountain wave signals. Both the gradient and the flux Richardson numbers are less than unity below 5 km MSL and increase to 2 near 5.5 km MSL. At the levels of the four KH legs, the mean Richardson numbers are relatively small but still larger than the critical Richardson number (i.e., ¼). This is consistent with the nearly laminar waves observed outside the first crest along the KH legs. The occurrence of KH eddies in the first wave crest likely results from the interaction between trapped waves and the stable shear layer between 4.5 and 5.5 km. As demonstrated in the appendix, a trapped wave can modify the local Richardson number by changing the vertical wind shear, static stability and vertical acceleration. In general, the Richardson number tends to be reduced in wave crests and the reduction is proportional to the wave amplitude. Although two wave crests are observed along these KH legs, the amplitude of the first wave is substantially larger than the second. Consequently, the local Richardson number should be smaller in the first wave crest where KH eddies and turbulence are observed.

c. Turbulence

Although the in-valley flight legs are predominantly turbulent in character, the filtered vertical velocity still

reveals the existence of wave signatures (>6 km), especially along the upper in-valley legs (i.e., above 3 km MSL). Large eddies are also apparent at all levels, indicative of complex multiscale interaction between turbulence and waves.

The mean vertical velocity $\overline{w}$, sensible heat flux Sflx ($=\overline{\rho}C_p\overline{\theta''_v w''}$), momentum Uflx ($=\overline{\rho}\overline{u''w''}$) flux, and turbulence kinetic energy per unit mass e [$=(\overline{u''^2 + v''^2 + w''^2})/2$; hereafter referred to as TKE for simplicity] are also shown in Fig. 4. Above the mountaintop level, the leg-mean vertical velocity is negative and on the order of 0.5 m s^{-1}, associated with mountain wave-induced descent in the lee of the Sierra ridge. In Owens Valley, the wave-induced mean vertical velocity is positive, probably associated with the ascending branch of the mountain waves.

Above 5.5 km MSL, the sensible heat and cross-valley momentum fluxes (wave contribution has been removed), and TKE are nearly zero, which is consistent with the laminar waves observed along the top three legs. For the KH and in-valley turbulence flight legs, the average sensible heat fluxes are negative, indicative of downward heat transfer by turbulence. The largest downward heat flux is observed along the lowest KH leg (i.e., ~4.6 km MSL), where the air is stable and turbulence is strong. The cross-valley momentum flux is negative in the valley, implying downward momentum mixing. As expected, the momentum flux amplitude also reaches a maximum approximately at 4.6 km MSL, where strong vertical wind shear and turbulence are present. A secondary maximum is located below the ridge crest, probably associated with wave-induced vertical wind shear. The TKE profile shows a maximum (~39 m^2 s^{-2}) near 4.6 km MSL, apparently associated with KH eddies. In the valley, TKE shows little variation with height, which reflects the presence of a deep turbulent layer in Owens Valley.

4. Breaking KH billows

The high-frequency variations superposed on the kilometer-scale eddies observed along legs 5–7 suggest that these eddies are overturning or breaking. In this section, we will further examine characteristics of these large eddies.

Within the first wave crest, kilometer-scale eddies oriented along the prevailing wind direction are evident in all four KH leg measurements (Fig. 3). However, the characteristics of small-scale turbulence observed along the four legs are substantially different. The top KH leg (i.e., leg 4) is characterized by four vertical velocity maxima within the first wave crest with a horizontal wavelength of approximately 2–3 km. Perturbations with wavelengths less than 500 m are negligible. Along leg 5, the kilometer-scale eddies are relatively smooth as well except for a few narrow turbulent zones (Fig. 3). The lower two KH legs (i.e., 6 and 7) are significantly more turbulent throughout the first wave crest. The coexistence of kilometer-scale eddies and small-scale turbulence observed along legs 5–7 is consistent with simulated breaking KH eddies in previous studies (e.g., Klaassen and Peltier 1985; Fritts et al. 1996). The difference in the characteristics of small-scale turbulence along legs 4–7 could be due to the intersection of the flight segments with the different portions of these breaking KH eddies. According to previous numerical studies (e.g., Klaassen and Peltier 1985; Fritts et al. 1996), breaking KH billows (eddies) are characterized by turbulent billow cores connected by less turbulent braids where secondary instability sometimes occurs. If the aircraft flight level is above the turbulent billow cores (e.g., leg 4), only large eddies are observed. For a flight leg that cuts through the top of the billow cores (e.g., leg 5), the aircraft samples large eddies separated by narrow turbulent zones where the flight leg intersects with the billow cores. The lower two flight legs (e.g., legs 6 and 7) observe KH eddies superposed with strong turbulence as they pass through turbulent billow cores.

To examine the structure and phase relations of these multiscale perturbations, the vertical velocity, cross-valley horizontal velocity, and potential temperature along legs 5–7 over a 15-km segment within the first wave crest are shown in Fig. 5. It is noteworthy that variations of the along-valley velocity component (i.e., normal to the flight-track component; not shown) associated with kilometer-scale eddies are much smaller than the cross-valley component. For leg 5, large eddies with a horizontal scale of approximately 2 km are evident in both the vertical velocity and the cross-valley wind component measurements (Fig. 5a). The corresponding vertical velocity range (i.e., estimated from the filtered curve) is approximately 6 m s^{-1} and the corresponding U variations are much smaller (~3 m s^{-1}). There seems to be an approximate 90° phase lag between w and U variations for these large eddies. The potential temperature variation is nearly 180° out of phase with the U variation and 90° out of phase with the vertical velocity. Although these KH eddies are highly nonlinear, linear theory may provide some useful qualitative insights into these phase relations. For a given horizontal wavenumber k the linear polarization relations between w, U, and θ perturbations can be written as (e.g., Nielsen 1992)

$$\hat{w}(k) = -\frac{kg}{\overline{\theta}N^2}[c_i + i(\overline{U} - c_r)]\hat{\theta}(k) \quad \text{and} \qquad (2)$$

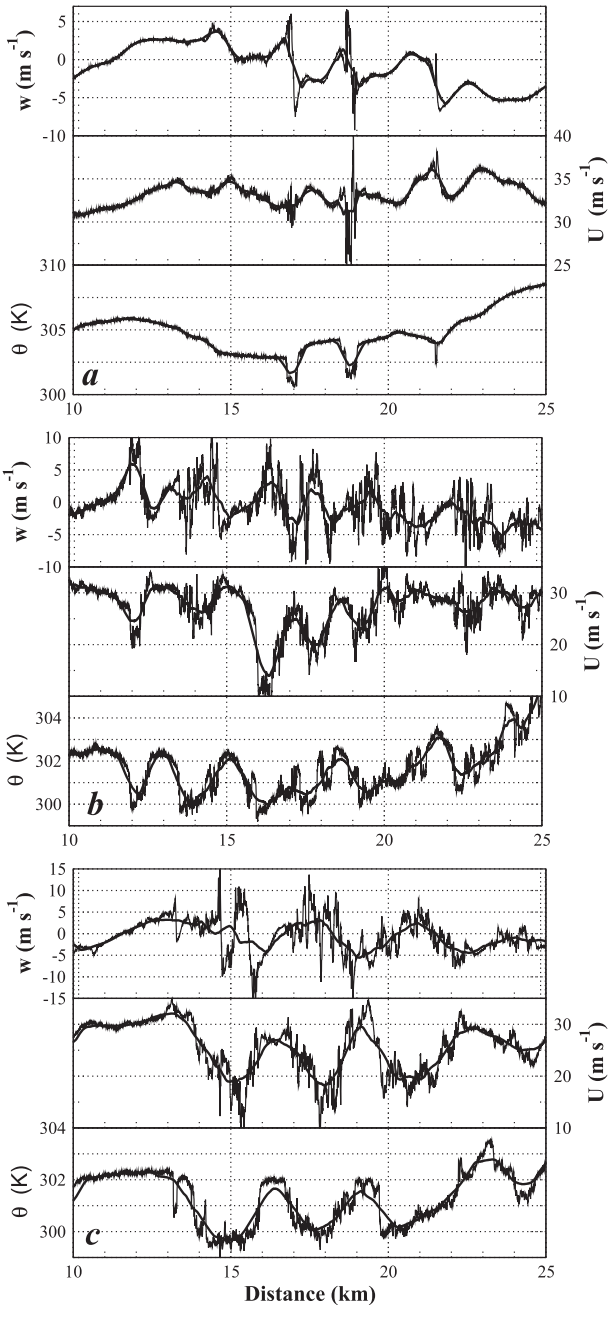

FIG. 5. Plots of w, U, and θ as a function of distance for the segment between 10 and 25 km for KH legs (a) 5, (b) 6, and (c) 7. The corresponding filtered curves are also included.

$$\hat{u}(k) = -\frac{m}{k}\hat{w}(k), \tag{3}$$

respectively, where $c = c_r + ic_i$ is the complex wave phase speed and $(\hat{w}, \hat{u}, \hat{\theta})$ denote the corresponding Fourier components of the (w, U, θ) variations. The vertical wavelength m is given by $m^2 = [N^2/(U-c)^2] - [(\partial^2 U/\partial z^2)/(U-c)] - k^2$.

Based on (2) and (3), the vertical velocity and potential temperature variations should be 90° out of phase for a neutral wave mode (i.e., $c_i = 0$), and for a neutral and propagating (i.e., $c_i = 0$ and $m^2 > 0$) wave, the phase lag between the vertical and horizontal velocity perturbations should be 180° (or −180°). The phase relations for kilometer-scale eddies observed along leg 5 are consistent with a propagating neutral plane wave with the phase line tilted westward with height.

Along leg 5, sharp perturbations appear in three narrow zones (~0.2–0.5 km wide) located near 17, 19, and 21.5 km, respectively, and the maximum w range of the high-frequency perturbations reaches approximately 16 m s^{-1} (Fig. 5a). In these turbulence zones, the vertical velocity perturbations associated with large eddies are nearly zero and the corresponding θ perturbations reach local minima, which is also consistent with the findings of Nielsen (1992) from aircraft observations of KH waves associated with a coastal frontal inversion. He noticed that velocities are "turbulent during the cold half of the wave and smoother during the warm half of the wave." For leg 6, several large eddies with two predominant horizontal scales of approximately 1 and 2 km are embedded in strong turbulence signals. Similarly, leg 7 is characterized by both strong turbulence and large eddies with a predominant horizontal scale of approximately 3.5 km. In general, for these kilometer-scale eddies, the U and θ variations appear to be approximately in phase with each other and approximately 180° out of phase with the w variations. These phase relations imply negative momentum and sensible heat fluxes associated with these eddies, the impact of which on large eddies can be seen from the TKE equation for a two-dimensional compressible flow:

$$\frac{De}{Dt} = -\overline{u'w'}\frac{\partial \overline{U}}{\partial z} + \frac{g}{\theta}\overline{w'\theta'} - \frac{\partial \overline{w'e'}}{\partial z} - \frac{1}{\overline{\rho}}\frac{\partial \overline{w'p'}}{\partial z} - \varepsilon, \tag{4}$$

where the right-hand terms correspond to shear production, buoyancy production, vertical turbulent transport, pressure correlation, and dissipation rate of TKE, respectively. According to (4), given a positive shear in the mean winds, a negative momentum flux indicates a positive TKE production rate and a negative heat flux tends to inhibit turbulence development. The turbulent transport and pressure correlation terms are typically small and difficult to estimate. To evaluate the relative importance of the first two terms for large eddies, we define $R(k)$ as the ratio of the first two terms in their spectral forms; that is,

$$R(k) = \frac{g}{\overline{\theta}}\frac{C_{w\theta}(k)}{C_{wu}(k)}\left(\frac{\partial \overline{U}}{\partial z}\right)^{-1}, \tag{5}$$

TABLE 2. Coh_{wu}, $\mathrm{Coh}_{w\theta}$, ϕ_{wu}, $\phi_{w\theta}$, C_{wu}, and $C_{w\theta}$ for λ derived from flight legs 5, 6, and 7. The corresponding $R(k = 2\pi/\lambda)$ values are included as well.

Leg	$\overline{U}$ (m s^{-1})	λ (km)	ϕ_{wu} (°)	Coh_{wu}	C_{wu} (m^2 s^{-1})	$\phi_{w\theta}$ (°)	$\mathrm{Coh}_{w\theta}$	$C_{w\theta}$ (K m)	$R(k)$
5	28	2.0	−105	0.98	−17.8	110	0.80	−8.1	1.5
6	27	1.3	−170	0.92	−170	−155	0.73	−12	0.24
7	24	3.5	165	0.80	−250	160	0.83	−50	0.66

where $C_{w\theta}$ and C_{wu} denote the cospectra of vertical velocity, potential temperature, and cross-valley velocity component variations. Note that $R(k)$ resembles a Richardson number and measures the relative amplitudes of the shear and buoyancy production of perturbation energy for a given k. When $R(k) < 1$, the shear production term dominates and eddies with k could grow by extracting mechanical energy from the mean flow to overcome the stratification effect. For legs 5–7, the dominant wavelengths $\lambda = 2\pi/k$ and the corresponding $R(k)$ values are calculated using Fourier transform and listed in Table 2. Taylor's hypothesis of "frozen" turbulence is used to convert the UWKA measurements from the frequency space into the wavenumber space. It is noteworthy that the UWKA tends to maintain a constant true airspeed along each flight leg; as a result, the ratio between the longitudinal velocity variations and the UWKA true airspeed is on the order of 10% or less. Therefore, although the large velocity variations associated with large-amplitude waves and turbulence observed during IOP 4a may have some effect on the accuracy of the estimated dominant eddy sizes, the Taylor hypothesis is still valid. The dominant wavenumbers are selected by identifying energy-containing peaks in velocity and potential temperature power spectra using the 25-Hz aircraft data over the 10–25-km segment in the first wave crest after removing the linear trend. It is interesting that the U, w, and θ variations are highly coherent for these wavenumbers. The corresponding V (i.e., along-valley component) variations are much smaller and the coherence (Coh) between V and w variations is generally below 0.4. This is consistent with two-dimensional KH billows, the axis of which is perpendicular to the wind shear.

For all three legs, the buoyancy tends to inhibit the growth of the identified eddies, as expected in a stably stratified flow. The phase relations between U and w allow eddies to extract energy from the positively sheared flow. For leg 5, the buoyancy effect dominates and the identified eddies are unable to grow even if the dissipation is negligible. Again, this is consistent with the hypothesis that leg 5 passes through the top of breaking KH eddies. Along legs 6 and 7 the $R(k)$ values are less than unity, indicating that the shear production of energy is large enough to overcome the buoyancy effect and the eddies are probably growing. It is also interesting that, using linear relations (2) and (3) and the phase angles between $\hat{w}$ and $\hat{\theta}$ in Table 2, we obtain that $c_i > 0$ for both legs 6 and 7, that $U - c_r > 0$ (i.e., disturbance drifts with the local flow) for leg 6, and that $U - c_r < 0$ for leg 7, implying that the steering level is probably located between legs 6 and 7. However, we should be cautious about applying linear theory to the observed KH eddies, which are highly nonlinear, especially for legs 6 and 7. Finally, we note that the observed largest eddy size is 3.5 km and the depth of the stable layer is approximately 0.5 km, and the ratio of the two is comparable to that of KH waves from previous studies (i.e., ~7.5; Miles and Howard 1964).

In summary, the characteristics of the kilometer-scale eddies observed along legs 4–7 are consistent with breaking KH billows described in previous studies (e.g., Klaassen and Peltier 1985; Nielsen 1992; Fritts et al. 1996). These eddies are not likely generated by breaking trapped waves. The wave nonlinearity index for trapped waves—$a = N|\eta|_{\max}/\overline{U}$, where $|\eta|_{\max}$ is the maximum vertical displacement for each leg—is relatively small for the wave and KH legs (Table 1), implying that nonlinear processes such as wave steepening and breaking contribute little to the eddy and turbulence generation.

5. Characteristics of large eddies and turbulence

The preliminary analysis of the KH and turbulence legs in the previous section reveals the coexistence of waves, large eddies, and small-scale turbulence from the lower to midtroposphere over Owens Valley. In this section, we examine further the characteristics of the observed eddies and turbulence using three different methods, namely, Fourier transform–based spectral analysis, wavelet analysis, and structure functions.

a. Spectral analysis

Previous studies have demonstrated that Fourier spectral analysis is a useful tool for scale separation and for identifying turbulence inertial subranges (e.g., Lilly and Lester 1974; Nastrom and Gage 1985, among others). As an example, the power spectra of the vertical and longitudinal velocity components and the potential temperature for leg 5 are shown in Fig. 6a. The 25-Hz data

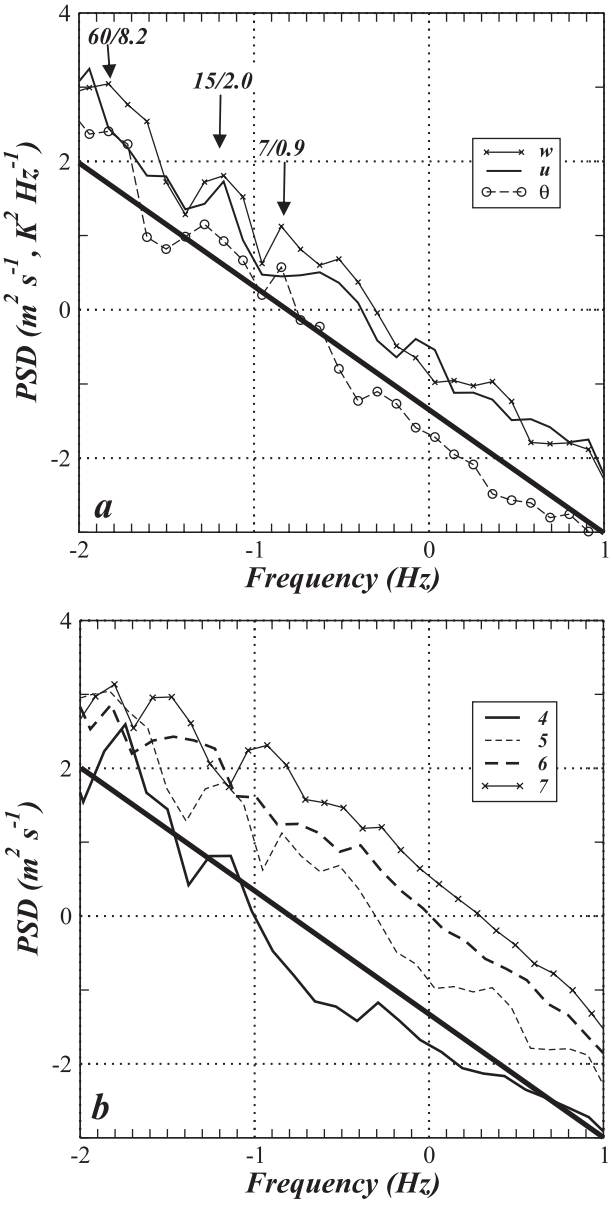

FIG. 6. (a) The power spectra density (PSD) of w, U' ($m^2\ s^{-1}$), and θ (K^2 s) as a function of frequency in log-coordinates for KH leg 5. The periods (s) and horizontal scales (km) corresponding to three energy-containing peaks are labeled. (b) The PSD of w for the four KH legs. The bold lines with slopes of $-5/3$ are included for comparison.

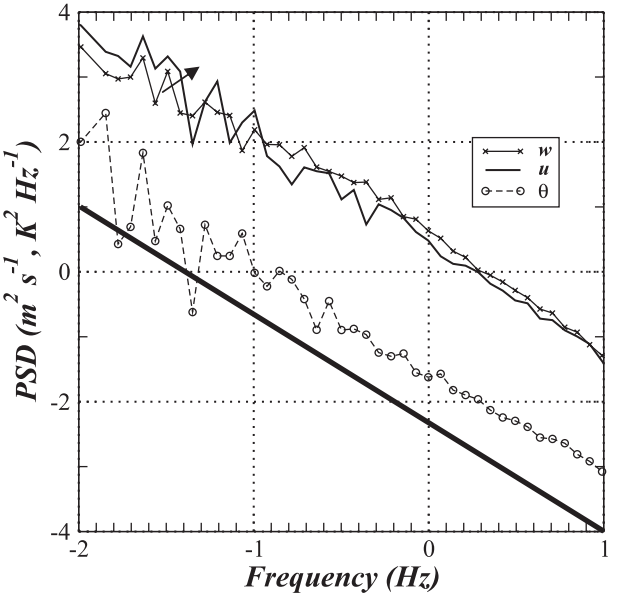

FIG. 7. As in Fig. 6a, but for flight leg 11.

have been linearly detrended before applying the Fourier transform, and the obtained spectra have been averaged over each equal-log interval [i.e., $\Delta\log(f) = 0.1$] of frequency. Only the portion between 0.01 and 10 Hz is shown. A number of maxima are evident in the power spectra of the u, w, and θ variations, implying the presence of multiscale waves and large eddies along the KH legs. For example, in the w spectrum of leg 5 there are three peaks, centered approximately at 8.2, 2.0, and 0.92 km, respectively, that satisfy the 95% confidence test (Bendat and Piersol 1986). Particularly, the 2.0-km maximum appears in all three spectra and the scale is comparable to the visual estimation of the KH eddy wavelength within the first wave crest (Fig. 3). The mean spectral slopes are approximately $-5/3$ over the high-frequency range, from 10 Hz up to approximately 0.05 Hz, which corresponds to approximately 2 km in length scale.

The w spectra of the four KH legs share some common characteristics such as multiple kilometer-scale energy-containing maxima (Fig. 6b). For the three lower KH legs, the mean power spectral slopes are approximately $-5/3$ for scales less than 2 km, suggestive of an inertial subrange. The spectrum of the top KH leg (i.e., leg 4) exhibits a mean slope gentler than $-5/3$ for higher frequencies. The lack of a well-defined inertial subrange in the spectra of the top KH leg is consistent with the weak high-frequency perturbations along this leg (Fig. 3). For turbulent legs below the mountaintop level, the power spectra follow the $-5/3$ power law from 10 Hz up to approximately 0.1 Hz (~1 km; Fig. 7), and multiple energy-containing maxima are evident over lower frequencies, corresponding to kilometer-scale eddies. The u and w spectra follow each other more closely, suggesting that the turbulence is more isotropic below the mountaintop level than at the KH leg levels.

b. Wavelet analysis

Wavelet analysis has been widely used for the study of intermittent turbulence and wave–turbulence interactions

(e.g., Argoul et al. 1989; Farge 1994; Demoz et al. 1998). Using wavelet analysis, localized turbulence structures can be readily revealed in a time period [(frequency)$^{-1}$] domain. In the following, orthonormal wavelet transformations are applied to the UWKA data to examine the turbulence energy distribution in both the flight time (space) and frequency for each leg. The mother wavelet we use here is the Morlet wavelet (Morlet et al. 1982), one of the most commonly applied in turbulence studies. Shown in Fig. 8 are the wavelet power spectra of the normalized vertical velocity perturbations w'/σ_w for five KH legs, where σ_w is the standard deviation of w. We only discuss signals above the white curves, which correspond to the 95% significance level.

Along these KH legs, the perturbation energy is largely contained in wave-scale motion, associated with the trapped waves (i.e., warm colors with time scale longer than 60 s in Fig. 8). For the top three KH legs, small-scale turbulence appears in the first wave crest, corresponding to the breaking KH eddies in Fig. 3. For example, along leg 5 there are energy maxima centered near 60 s (~8 km) and 16 s (~2 km) in frequency, which is consistent with the power spectrum of w in Fig. 6a. The 2-km maximum splits into four vertically oriented conelike patches pointing toward higher frequencies, suggesting downscale energy cascade. For the lower KH legs, nearly equally spaced cones are evident and the small-scale turbulence becomes progressively stronger. It is noteworthy that these conelike energy maxima are characterized by distinctive maxima in frequency rather than by a gradual decrease toward higher frequency, which is consistent with the presence of multiple energy-containing peaks in the power spectra (Fig. 6b). This implies that frequency preferences exist in the downscale energy cascade associated with the breakdown of KH eddies. Figure 8 also indicates that the turbulence tends to develop in the second wave crest along the two lower KH legs. However, the turbulence is much less pronounced in strength and less organized than in the first wave crest.

For turbulence legs, small-scale turbulence is nearly uniformly distributed, implying that the turbulence is more fully developed in the valley than at the KH levels. The vertically oriented coherent conelike structures are not as evident as in the KH legs. However, energy-containing large eddies (i.e., scales between 0.5–6 km) are evident along all the legs. Specifically, some vertically coherent large eddies (Fig. 8) are located over the eastern side of the valley, probably associated with wave breaking.

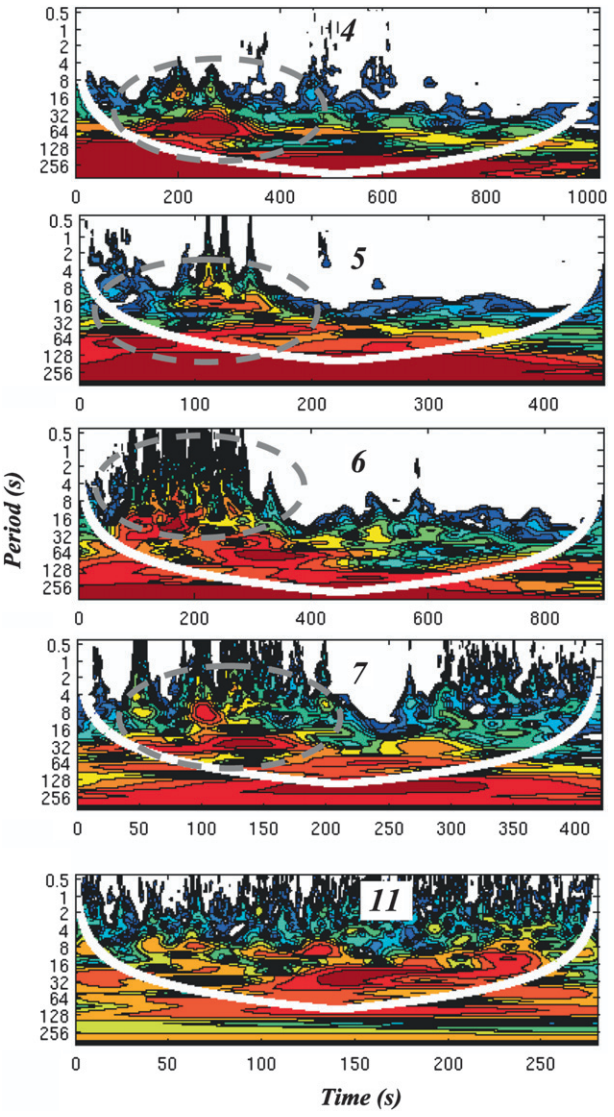

FIG. 8. The wavelet spectra of w (normalized by its variance) for the four KH flight legs and a turbulence leg are shown. The time (s) is labeled from west to east on abscissa and the period [i.e., (frequency)$^{-1}$] is shown in a logarithmic scale. The power spectra are color filled as 2^n, with n = 0, 1, 2, 3, 4, 5, 6, and 7, corresponding to cold to warm colors. The white curves correspond to 95% significance level. The flight leg numbers are labeled. The locations of the first wave crest are highlighted by dashed ellipses for the KH legs.

c. *Structure functions*

In this section, second- and third-order structure functions for each leg are evaluated to further examine the turbulence characteristics. The one-dimensional second-order structure function of a generic variable ϕ is defined as

$$D_{\phi\phi}(r) = \langle(\delta\phi')^2\rangle, \tag{6}$$

where $\delta\phi' = \phi'(x + r) - \phi'(x)$, $\phi' = \phi - \overline{\phi}$ is the perturbation of ϕ relative to the mean value $\overline{\phi}$, x is the longitudinal axis, r is the separation distance, and the

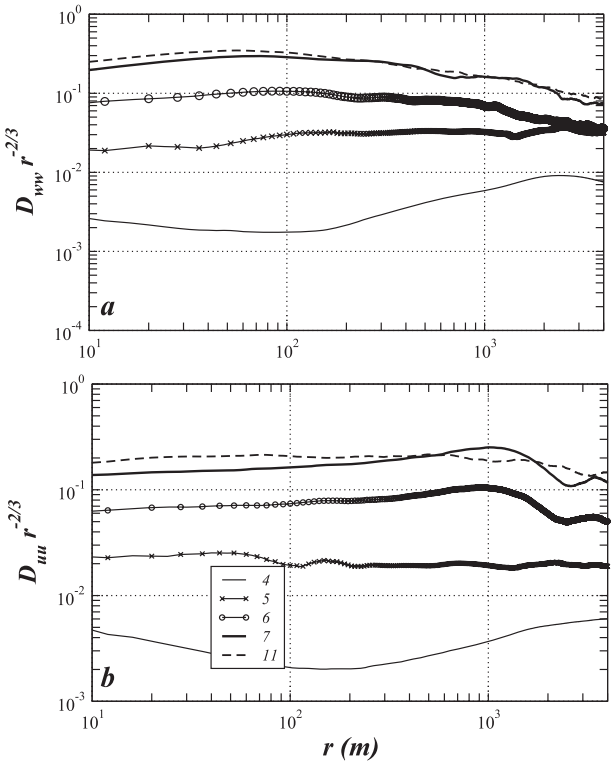

FIG. 9. The normalized second-order structure functions (a) $D_{ww}r^{-2/3}$ and (b) $D_{uu}r^{-2/3}$ for the four KH legs and leg 11 of IOP 4a are plotted as a function of the separation distance.

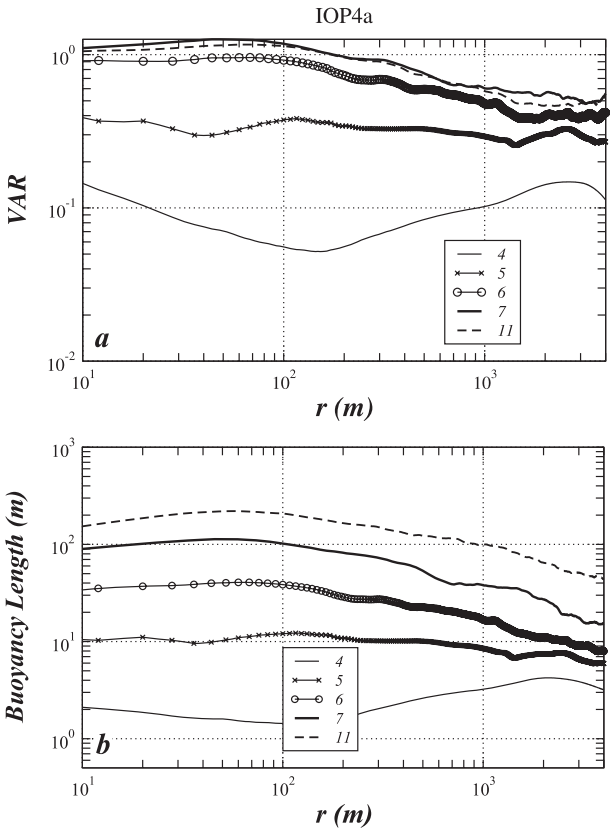

FIG. 10. (a) VAR defined by (6) and (b) the buoyancy length [(7)] for five IOP 4a legs (i.e., 4–7 and 11) are plotted as a function of separation distance.

angle brackets represent arithmetic averaging. In the inertial subrange, the second-order structure functions of the velocity components u, v, and w can be scaled as $D_{uu}, D_{vv}, D_{ww} \sim r^{2/3}$. The second-order structure functions of the longitudinal and vertical velocity components normalized by $r^{2/3}$ (i.e., $\hat{D}_{uu} = D_{uu}r^{-2/3}$ and $\hat{D}_{ww} = D_{ww}r^{-2/3}$) are shown in Fig. 9. It is evident that both $\hat{D}_{ww}$ and $\hat{D}_{uu}$ are approximately constant from the smallest resolvable scale up to 1 km for the lower three KH legs and the turbulence leg, which is consistent with the scaling in the inertial subrange. For $r > 1$ km, these curves drop off with further increase of r. This is in general agreement with the inertial subrange identified from the power spectra in Figs. 6 and 7. For the wave legs (not shown) and the top KH leg, $D_{ww}(r)r^{-2/3}$ decreases with an increase in r for$r$ $r < 200$ m, implying that the inertial subrange for the wave legs is not resolvable (i.e., less than 10 m), which is consistent with the absence of the $-2/3$ power law in the corresponding power spectrum (Fig. 6b). The kilometer scale energy-containing peaks shown in the power spectra are much less obvious in the corresponding $\hat{D}_{ww}$ and $\hat{D}_{uu}$. As pointed out by Mahrt and Gamage (1987), an energy peak in power spectra tends to spread over a range of separation distances in a structure function.

A pair of useful turbulence indices can be derived using the second-order structure functions, namely the velocity aspect ratio VAR(r) and the turbulence buoyancy length $L(r)$, defined as (Mahrt and Gamage 1987)

$$\mathrm{VAR}(r) = 2D_{ww}(r)/[D_{uu}(r) + D_{vv}(r)] \quad \text{and} \quad (7)$$

$$L(r) = D_{ww}(r)\Big/\left[\frac{g}{\bar{\theta}}\sqrt{D_{\theta\theta}(r)}\right], \quad (8)$$

respectively, where D_{vv} and $D_{\theta\theta}$ are the second-order structure functions of the along-valley velocity component and potential temperature. For legs 7 and 11, VAR is near unity for $r < 100$ m and decreases to approximately 0.5 for $r = 1$ km, implying that the small-scale turbulence is nearly isotropic, and large eddies are more horizontal because of the stratification effect (Fig. 10). The velocity aspect ratios are much smaller for the wave legs (not shown) and increase with decreasing altitude for the four KH legs. The buoyancy length for the top KH leg is much smaller than other legs because of the stronger stratification aloft (Fig. 2). In general, the buoyancy length increases with decreasing altitude for legs

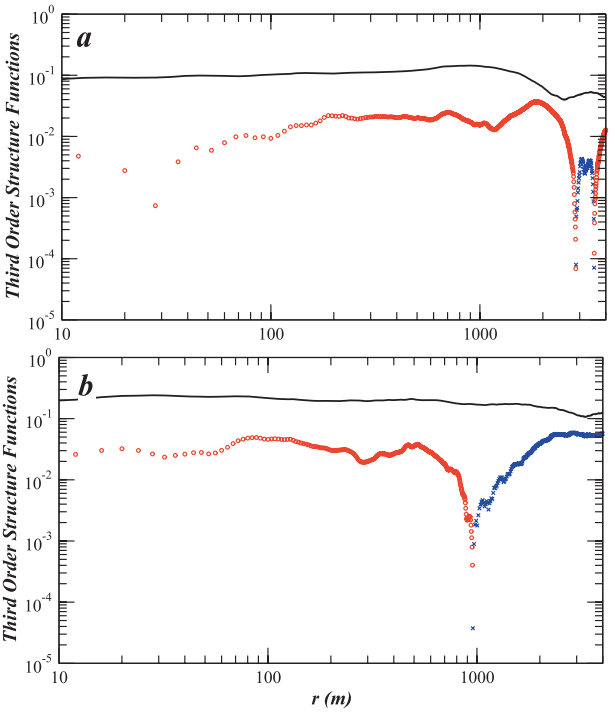

FIG. 11. The normalized third-order structure functions are plotted vs r for legs (a) 6 and (b) 11. The bold solid curve, red circles, and blue crosses correspond to S_3/r, $\hat{D}_{uu_Tu_T}$, and $-\hat{D}_{uu_Tu_T}$ (when $\hat{D}_{uu_Tu_T} < 0$), respectively.

1–10, reaches a maximum at leg 11 (~3300 m), and then decreases further with decreasing altitude.

In the remainder of this section, we evaluate three third-order structure functions for each flight segment, namely, the third-order absolute structure function of the longitudinal velocity S_3, defined as

$$S_3 = \langle |\delta u(r)|^3 \rangle; \tag{9}$$

the third-order structure function $D_{uu_Tu_T}$, defined by

$$D_{uu_Tu_T} = \langle (\delta u)^3 \rangle + 2\langle \delta u (\delta u_T)^2 \rangle, \tag{10}$$

where $\langle (\delta u_T)^2 \rangle = [\langle (\delta v)^2 \rangle + \langle (\delta w)^2 \rangle]/2$; and the structure skewness, defined as

$$S_w(r) = D_{www}/(D_{ww})^{3/2}, \tag{11}$$

where $D_{www} = \langle (\delta w)^3 \rangle$. In the turbulence inertial subrange, S_3 is proportional to r (Cho et al. 2001) and $D_{uu_Tu_T} = -4\langle \varepsilon \rangle r/3$ (Lindborg 1996; Antonia et al. 1997). The sign of $D_{uu_Tu_T}$ indicates the direction of the turbulence energy cascade (Frisch 1995; Lindborg 1996); the energy cascade is downscale if $D_{uu_Tu_T}$ is negative (i.e., $\langle \varepsilon \rangle > 0$ or a positive dissipation rate) and upscale if it is positive (i.e., a negative dissipation rate). The structure skewness is

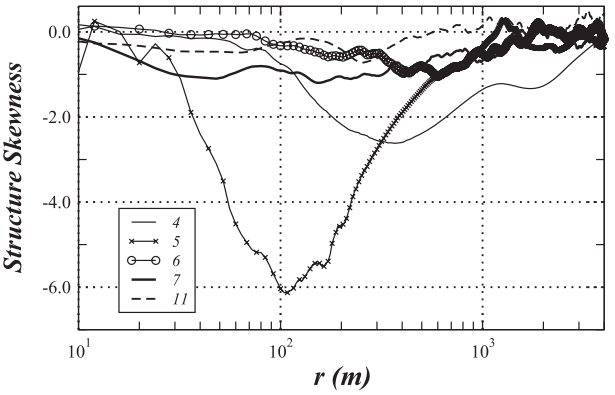

FIG. 12. The structure skewness is plotted as a function of separation distance for the four KH legs and the turbulence leg 11.

negative if the shear generation of turbulence dominates (Mahrt and Gamage 1987).

Figure 11 shows S_3/r and $\hat{D}_{uu_Tu_T} = -3D_{uu_Tu_T}/4r$ for the four KH and one turbulence flight segments. Over turbulence inertial subranges, these functions should be constant with r and $\hat{D}_{uu_Tu_T}$ should be equal to the mean turbulence dissipation rate. For leg 6, the normalized third-order structure functions are approximately constant for r between 100 and 1000 m, an inertial subrange identified from spectral and second-order structure function analysis. It is noteworthy that the turbulence dissipation rate is negative between 2900 and 3500 m (Fig. 11a), indicative of a possible upscale energy transfer. The negative dissipation rates are found for some of the turbulence legs as well (Table 1). For example, for leg 11, the turbulence dissipation rate is negative for scales of 1 km or longer (Fig. 11b).

The KH legs are characterized by large negative structure skewness (Fig. 12), suggesting that the turbulence above the mountaintop is primarily shear generated, which is consistent with the velocity and Richardson number profiles (Figs. 2 and 4). From the smallest resolvable scale to 1 km, the skewness functions for the upper-turbulence legs are negative as well, with much smaller amplitude than the KH legs, associated with a weaker but well-defined forward wind shear. For some low-turbulence legs (~2500 m or lower; not shown) the skewness function oscillates near zero, indicating that the shear effect is weak and buoyancy generation of turbulence may be important at these levels.

Finally, it is worth noting that turbulence over complex terrain is inhomogeneous in nature. Consequently, the average over each flight leg, with substantial variability in turbulence characteristics, may not necessarily represent local turbulence statistics in a quantitative sense. This is especially true for the spectral and structure function analysis and is less of a problem for wavelet analysis.

6. Comparisons between IOPs 1a and 4a

Large eddies embedded in shear layers and trapped waves have been documented during several other T-REX flights in addition to IOP 4a. Among them, IOP 1a is the only flight that documented vertically coherent KH eddies along three or more flight legs above the mountaintop level. For the sake of generality, in this section we will examine the IOP 1a flight and discuss similarities and differences of the turbulence characteristics observed during these two flights.

The large-scale flow conditions for IOPs 1a and 4a are quite similar. The cross-valley wind profile is characterized by weak winds below 3 km MSL, a strong shear layer between 3 and 5 km, and strong winds aloft (Fig. 13). In the shear layer, the mean and maximum vertical wind shears are 0.01 and 0.015 s^{-1}, respectively, and the gradient Richardson number is less than unity. The atmosphere has greater static stability below 3 km and becomes gradually less stable aloft. Consequently, the Scorer parameter exhibits a sudden decrease between 3 and 4 km, which favors the formation of trapped waves.

UWKA observed relatively steady trapped waves as indicated by the vertically coherent wave patterns (Fig. 14). The EQR values computed from wave legs 1–4 are respectively 0.99, 0.54, 0.37, and 0.32, implying that the waves are trapped below approximately 8.5 km MSL (Table 3). The wavelength and wave amplitude (i.e., in terms of w) are comparable to those observed in IOP 4a. For the three legs between 4.5 and 6 km MSL, clusters of sporadic perturbations are evident in the second wave crest, which is centered over Owens Valley and has substantially larger amplitude in terms of the vertical displacement than the first and third wave crests (Fig. 14). Again, this suggests that wave-induced KH instability only occurs when the wave amplitude exceeds a certain threshold. Similar to IOP 4a, the KH at the highest altitude leg is also characterized by relatively smooth kilometer-scale eddies separated by narrow turbulent zones, probably resulting from the intersection of the flight segment with the undular top of breaking KH billows. Along the two lower KH legs, kilometer-scale eddies are evident within the second wave crest, embedded in strong turbulence. The wavelet spectra of the three KH legs for IOP 1a also exhibit the vertically coherent conelike structures with distinctive maxima in period. These "cones" point toward smaller scales, suggestive of a predominant downscale energy cascade (Fig. 15). Small-scale turbulence and large eddies are evident in the wavelet spectra of the turbulence leg below the mountaintop and these large eddies are primarily shear-induced, probably associated with the interaction between waves and in-valley flows. It is evident that the nonlinear

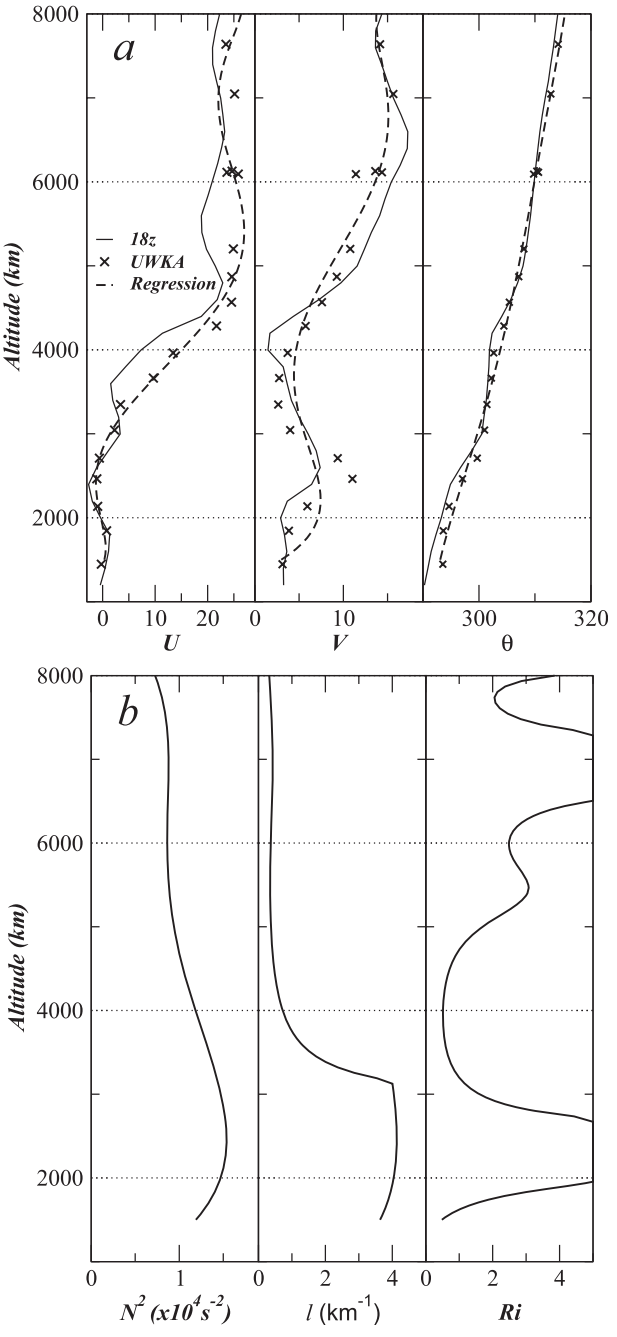

FIG. 13. (a) Profiles of the cross-valley and along-valley wind components (i.e., U and V) and potential temperature derived from the 1800 UTC 2 Mar 2006 NCAR ISS sounding and UWKA measurements. (b) The buoyancy frequency squared, Scorer parameter, and gradient Richardson number derived from the sixth-order polynomial regressions.

index $N\eta/U$ becomes significantly larger below the mountaintop level where the cross-valley winds are much weaker (Table 3). As demonstrated in previous studies, for highly nonlinear waves, turbulence could

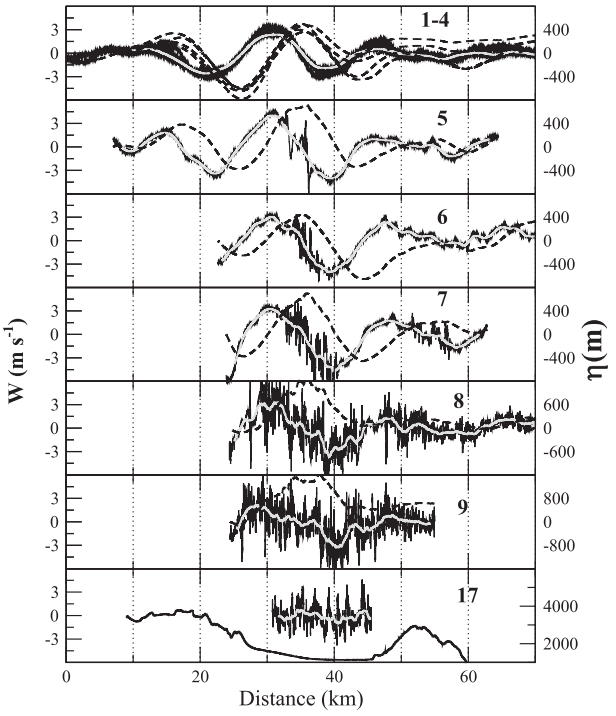

FIG. 14. The 25-Hz vertical velocity for IOP 1a is plotted as a function of the horizontal distance from a reference point over the Sierra ridge (the west end-point of the top leg) for legs (top)–(bottom) 1–9 and 17, including topography. The corresponding vertical displacement and filtered vertical velocity curves are shown as dashed and gray curves, respectively.

extract energy from waves associated with nonlinear processes such as wave steepening or breaking (Fua et al. 1982; Weinstock 1986). The interaction between trapped waves and a stagnant layer beneath a stable shear layer has been examined by Jiang et al. (2006). Using a mesoscale model, they demonstrated that turbulence develops in an initially nonturbulent shear or stagnant layer beneath the first few wave crests, and the trapped waves decay with downstream distance.

For the IOP 1a flight, the third-order structure functions shown in Fig. 16 suggest a possible upscale energy transfer along both the KH and in-valley turbulence legs with horizontal scales ranging from a few hundred meters to a few kilometers. The horizontal scale ranges in which the upscale energy transfer may occur are included in Table 3. Negative dissipation rates or upscale energy transfer have been documented by previous studies for scales between 500 and 1000 km, which has been interpreted using the two-dimensional turbulence theory or attributed to the Coriolis effect (Högström et al. 1999; Cho et al. 2001). More recently, Koch et al. (2005) analyzed aircraft measurements of turbulence associated with gravity waves excited by a frontal system. Negative energy dissipation was found for horizontal scales from

TABLE 3. As in Table 1, but for IOP 1a.

Leg	Time (UTC)	Alt (m)	Char	Data points	a	Upscale range (m)
1	1659–1708	8550	Wave	14 275	0.25	450 up
2	1711–1724	7640	Wave	19 025	0.23	430–830
3	1726–1734	7050	Wave	12 025	0.23	—
4	1736–1750	6110	Wave	21 025	0.23	—
5	1753–1800	5200	KH	11 275	0.27	530 up
6	1803–1814	4870	KH	17 275	0.26	—
7	1815–1820	4570	KH	8275	0.29	—
8	1824–1834	4280	Turb	15 525	0.58	—
9	1835–1840	3960	Turb	7525	1.3	—
10	1841–1847	3660	Turb	9775	2.5	—
11	1848–1851	3350	Turb	4525	—	300–730
12	1852–1856	3040	Turb	6025	—	3500 up
13	1857–1900	2710	Turb	3775	—	200 up
14	1901–1904	2460	Turb	5275	—	—
15	1905–1908	2140	Turb	4775	—	1700–2200
16	1909–1912	1840	Turb	4525	—	250 up
17	1913–1916	1450	Turb	4525	—	280 up

300 to 700 m, although no physical explanation was proposed. According to the wavelet analysis, the downscale energy cascade associated with KH instability exhibits scale preferences and generates distinctive energy maxima at different scales. The energy cascade associated with steepening or breaking mountain waves may have similar characteristics (Weinstock 1986; Jiang and Doyle 2004; Doyle et al. 2005). In contrast to classical phenomenological turbulence theory, which assumes steady forcing (i.e., energy source) in the large- or small-scale limit, the energy maxima associated with KH- or wave breaking–generated large eddies may serve as transient energy sources and disperse energy toward both larger and smaller scales.

7. Summary

The in situ measurements from two UWKA flights over Owens Valley during the Terrain-Induced Rotor Experiment have been analyzed with a focus on wave-induced KH instability and turbulence characteristics in the lower to middle troposphere over complex terrain. The two events examined are characterized by interaction between a stably stratified shear layer above the mountaintop level and stationary moderate-amplitude trapped waves. According to the observations and linear analysis, KH instability develops in the crests of trapped waves where the Richardson number is substantially reduced. KH-like eddies are absent in wave troughs, where the local Richardson number is increased. Wave-induced KH instability also shows wave amplitude dependence. In both IOPs, the KH eddies are observed in the wave crest with the largest wave amplitude, implying that KH

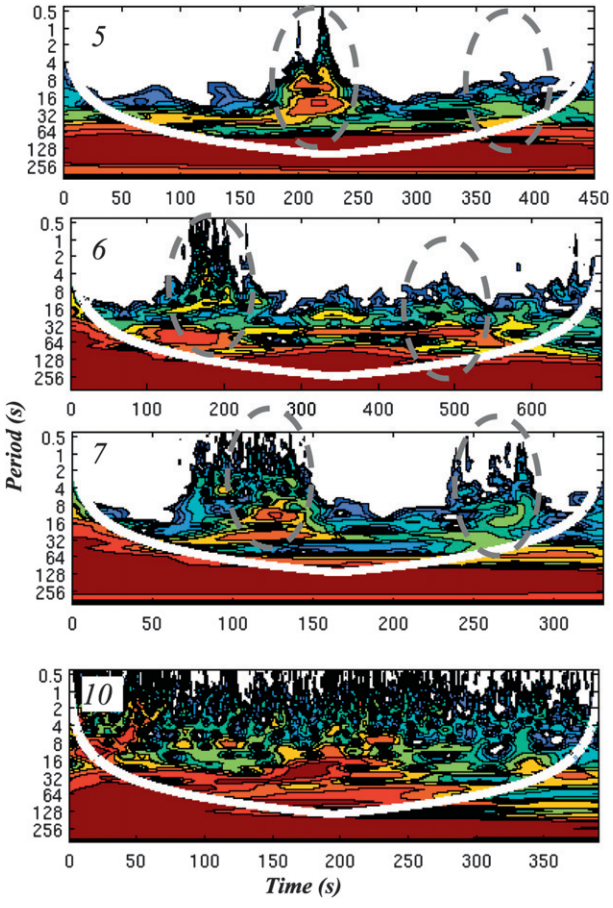

FIG. 15. As in Fig. 8, but for the three KH legs and a turbulence leg (i.e., leg 10) of IOP 1a. The locations of the second and third wave crests are highlighted by dashed ellipses.

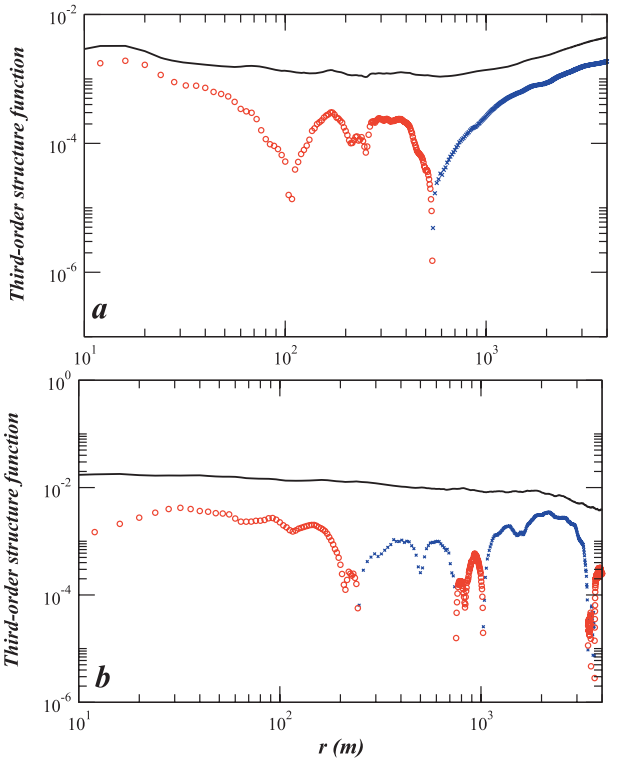

FIG. 16. As in Fig. 11, but for legs (a) 5 and (b) 16 of IOP 1a.

instability tends to develop only when the wave amplitude exceeds a certain threshold.

The phase relations between different velocity components and potential temperature for the observed kilometer-scale eddies are consistent with growing KH billows, suggesting that these eddies could extract energy directly from the sheared mean flow. The coexistence of large eddies and strong turbulence observed along some of the KH legs suggests those KH billows are likely breaking. The energy cascade associated with the breaking KH billows exhibits scale preferences and results in distinctive maxima in period (or wavelength) in the Fourier power spectra and wavelet spectra. For KH legs characterized by small-scale turbulence embedded in kilometer-scale eddies, the mean spectral slope becomes $-5/3$ for scales up to 1–2 km, which is consistent with the turbulence inertial subrange scaling. It is noteworthy that the corresponding second- and third-order absolute structure functions are also consistent with the inertial subrange scaling over a similar separation distance. The analysis of third-order structure functions suggests a possible upscale energy transfer on scales from a few hundred meters to a few kilometers, possibly associated with the transient energy dispersion from breaking large eddies generated by KH instability. These KH eddies are generally anisotropic with the vertical to horizontal aspect ratio less than unity because of the stratification effect. They are characterized by large negative skewness, indicative of strong asymmetry in updrafts and downdrafts associated with the positive vertical wind shear. It is noteworthy that large eddies were also observed below the mountaintop level during T-REX IOP 13 (Doyle et al. 2009). Those eddies, or subrotors, were induced by shear instability associated with an elevated horizontal vortex sheet generated through boundary layer separation (Doyle et al. 2009).

Below the mountain top level, vigorous turbulence is probably developing because of interaction with trapped waves aloft, which may have caused the fast decay of the trapped waves downstream. Turbulence extracts energy from waves through nonlinear wave steepening or wave breaking processes in accordance with the relatively weak cross-valley winds below the mountain top level. The associated energy cascade is predominantly downscale, but with scale preferences that result in a number of kilometer-scale energy-containing maxima in

the power spectra and wavelet spectra. Similar to KH eddies, these distinctive energy maxima may serve as transient energy sources and transfer energy toward both larger and smaller scales. In general, the turbulence below the mountaintop level is better developed and more isotropic than that at the KH levels, and it generally follows the $-5/3$ power law for scales less than 1 km.

Acknowledgments. The primary sponsor of T-REX is the U.S. National Science Foundation. The authors want to thank University of Wyoming King-Air flight staff and Dr. Larry Armi at Scripps Institution of Oceanography for their contributions to King-Air data collection. The first and second authors acknowledge support through Office of Naval Research Program Element 0601153N. V. Grubišić and R. B. Smith were supported by NSF through Grants ATM-0524891 and ATM-0531212, respectively. The first author has greatly benefited from discussions with Drs. Shouping Wang at the Naval Research Laboratory, Larry Oolman at University of Wyoming, Qing Wang from the Naval Postgraduate School, and Larry O'Neill from the National Research Council.

APPENDIX

Richardson Number Modified by a Trapped Wave

Consider the interaction between a shear layer characterized by a constant buoyancy frequency N and a linear shear U_z = constant and a simple stationary wave trapped between two rigid lids located at $mz = \pm\pi/2$ in an x–z plane. The vertical velocity induced by the trapped wave can be written as $w'(x, z) = w_0 \cos(mz) \cos(kx)$, where m and k are the vertical and horizontal wavenumbers, respectively, and w_0 is the maximum vertical motion. The ambient Richardson number is $\mathrm{Ri}_o = N^2/U_z^2$. Using linear theory, we obtain the horizontal velocity and potential temperature perturbations u' and θ' and the vertical displacement η:

$$\eta(x, z) = \frac{w_0}{Uk} \cos(mz) \sin(kx), \tag{A1}$$

$$u'(x, z) = \frac{mw_0}{k} \sin(mz) \sin(kx), \quad \text{and} \tag{A2}$$

$$\theta'(x, z) = -\frac{w_0 \overline{\theta}_z}{Uk} \cos(mz) \sin(kx). \tag{A3}$$

Assuming $\theta'_z/\overline{\theta}_z$, $2u'_z/U_z$, $g'/g \ll 1$, where $g' = Uw_x$ denotes the wave-induced vertical acceleration, to the first-order approximation, the local gradient Richardson number can be written as

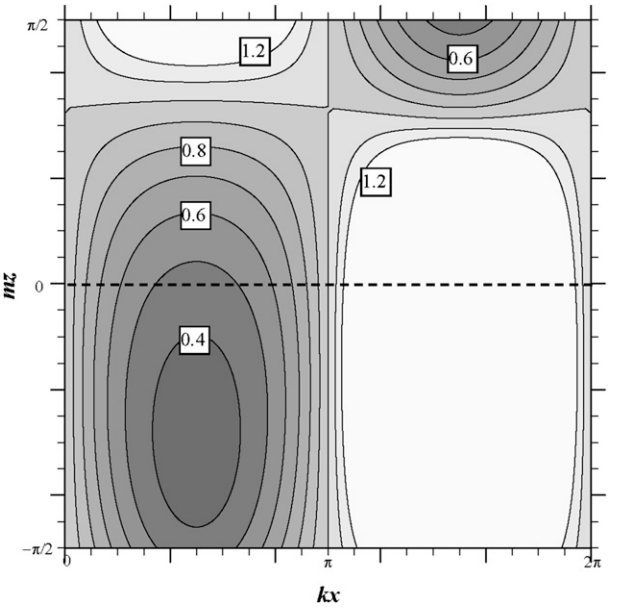

FIG. A1. The local Richardson number computed using (A4) is contoured. The contour interval is 0.1. Relevant parameters used in this example can be found in the appendix.

$$\mathrm{Ri}(x, z) = \mathrm{Ri}_o \left(1 + \frac{\theta'_z}{\overline{\theta}_z} - \frac{2u'_z}{U_z} + \frac{g'}{g}\right). \tag{A4}$$

The last three terms in the brackets correspond to wave-induced stability variation, shear variation, and wave-induced vertical acceleration effects, respectively. Using (A1)–(A4), we obtain

$$\mathrm{Ri}(x, z) = \mathrm{Ri}_o + \mathrm{Ri}_o \eta \left[\frac{U_z}{U} + m \tan(mz) - \frac{2m^2 U}{U_z} - \frac{k^2 U^2}{g}\right]. \tag{A5}$$

Equation (A5) indicates that both the wave-induced shear and vertical acceleration (i.e., last two terms in the brackets) tend to reduce the local Richardson number in a wave crest (i.e., $\eta > 0$) and act in the opposite sense in a wave trough. In addition, the Richardson number variation is proportional to the wave amplitude.

As an example, we use a set of parameters estimated from IOP 4a: $w_0 = 6$ m s^{-1}, $U_z = 0.013$ s^{-1}, $k = 3.14 \times 10^{-4}$ m^{-1}, $U(0) = 20$ m s^{-1}, and $N = 0.013$ s^{-1}, which yields $\mathrm{Ri}_o = 1$. The local Richardson number computed using (A5) and $m = \sqrt{(N/U)^2 - k^2}$ is shown in Fig. A1. It is evident that the Richardson number is substantially reduced within the wave crest and the lower half of the wave (i.e., $z < 0$), and Ri is increased in wave troughs. The Richardson number minimum is located at $\eta = \eta_{\max}$ and

$mz \approx -\pi/4$. The relative importance of wave-induced shear to acceleration can be expressed as $m^2g/(k^2UU_z)$. For the given example, the acceleration term is much smaller than the other three terms.

REFERENCES

Antonia, R. A., M. Ould-Rouis, F. Anselmet, and Y. Zhu, 1997: Analogy between predictions of Kolmogorov and Yaglom. *J. Fluid Mech.,* **332,** 395–409.

Argoul, F., A. Arnéodo, G. Grasseau, Y. Gagne, E. J. Hopfinger, and U. Frisch, 1989: Wavelet analysis of turbulence reveals the multifractal nature of the Richardson cascade. *Nature,* **338,** 51–53.

Bendat, J. S., and A. G. Piersol, 1986: *Random Data Analysis and Measurement Procedures*. John Wiley, 566 pp.

Cho, J. Y. N., B. E. Anderson, J. D. W. Barrick, and K. L. Thornhill, 2001: Aircraft observations of boundary layer turbulence: Intermittency and the cascade of energy and passive scalar variance. *J. Geophys. Res.,* **106,** 32 469–32 479.

Demoz, B. B., D. O'C. Starr, K. R. Chan, and S. W. Bowen, 1998: Wavelet analysis of dynamical processes in cirrus. *Geophys. Res. Lett.,* **25,** 1347–1350.

Doyle, J. D., M. A. Shapiro, Q. Jiang, and D. L. Bartels, 2005: Large-amplitude mountain wave breaking over Greenland. *J. Atmos. Sci.,* **62,** 3106–3126.

——, V. Grubišić, W. O. J. Brown, S. F. J. De Wekker, A. Dörnbrack, Q. Jiang, S. Mayor, and M. Weissmann, 2009: Observations and numerical simulations of subrotor vortices during T-REX. *J. Atmos. Sci.,* **66,** 1229–1249.

Farge, M., 1994: Wavelets and two-dimensional turbulence. *Computational Fluid Dynamics '94: Proceedings of the Second European Computational Fluid Dynamics Conference, 5–8 September 1994, Stuttgart, Germany,* Vol. I, S. Wagner, J. Périaux, and E.-H. Hirschel, Eds., John Wiley & Sons, 1–23.

Frisch, U., 1995: *Turbulence: The Legacy of A. N. Kolmogorov*. Cambridge University Press, 296 pp.

Fritts, D. C., T. L. Palmer, Ø. Andreassen, and I. Lie, 1996: Evolution and breakdown of Kelvin–Helmholtz billows in stratified compressible flows. Part I: Comparison of two- and three-dimensional flows. *J. Atmos. Sci.,* **53,** 3173–3191.

Fua, D., G. Chimonas, F. Einaudi, and O. Zeman, 1982: An analysis of wave–turbulence interaction. *J. Atmos. Sci.,* **39,** 2450–2463.

Grubišić, V., and Coauthors, 2008: The Terrain-Induced Rotor Experiment: A field campaign overview including observational highlights. *Bull. Amer. Meteor. Soc.,* **89,** 1513–1533.

Högström, U., A.-S. Smedman, and H. Bergström, 1999: A case study of two-dimensional stratified turbulence. *J. Atmos. Sci.,* **56,** 959–976.

Howard, L. N., 1961: Note on a paper of John W. Miles. *J. Fluid Mech.,* **10,** 509–512.

Jiang, Q., and J. D. Doyle, 2004: Gravity wave breaking over the Central Alps: Role of complex terrain. *J. Atmos. Sci.,* **61,** 2249–2266.

——, and ——, 2008: Diurnal variation of downslope winds in Owens Valley during the Sierra Rotor Experiment. *Mon. Wea. Rev.,* **136,** 3760–3780.

——, ——, and R. B. Smith, 2006: Interaction between trapped waves and boundary layers. *J. Atmos. Sci.,* **63,** 617–633.

Klaassen, G. P., and W. R. Peltier, 1985: Evolution of finite-amplitude Kelvin–Helmholtz billows in two spatial dimensions. *J. Atmos. Sci.,* **42,** 1321–1339.

Koch, S. E., and Coauthors, 2005: Turbulence and gravity waves within an upper-level front. *J. Atmos. Sci.,* **62,** 3885–3908.

Lilly, D. K., 1978: A severe downslope windstorm and aircraft turbulence event induced by a mountain wave. *J. Atmos. Sci.,* **35,** 59–77.

——, and P. F. Lester, 1974: Waves and turbulence in the stratosphere. *J. Atmos. Sci.,* **31,** 800–812.

Lindborg, E. A., 1996: A note on Kolmogorov's third-order structure-function law, the local isotropy hypothesis and the pressure–velocity correlation. *J. Fluid Mech.,* **326,** 343–356.

Mahrt, L., and N. Gamage, 1987: Observations of turbulence in stratified flow. *J. Atmos. Sci.,* **44,** 1106–1121.

Miles, J. W., 1961: On the stability of heterogeneous shear flows. *J. Fluid Mech.,* **10,** 496–508.

——, and L. N. Howard, 1964: Note on a heterogeneous shear flow. *J. Fluid Mech.,* **20,** 331–336.

Morlet, J., G. Arens, E. Fourgau, and D. Giard, 1982: Wave propagation and sampling theory. Part I: Complex signal and scattering in multilayered media. *Geophysics,* **47,** 203–221.

Nastrom, G. G., and K. S. Gage, 1985: A climatology of atmospheric wavenumber spectra of wind and temperature observed by commercial aircraft. *J. Atmos. Sci.,* **42,** 950–960.

Nielsen, J. W., 1992: In situ observations of Kelvin–Helmholtz waves along a frontal inversion. *J. Atmos. Sci.,* **49,** 369–386.

Scorer, R. S., 1949: Theory of waves in the lee of mountains. *Quart. J. Roy. Meteor. Soc.,* **75,** 41–56.

Smith, R. B., B. K. Woods, J. Jensen, W. A. Cooper, J. D. Doyle, Q. Jiang, and V. Grubišić, 2008: Mountain waves entering the stratosphere. *J. Atmos. Sci.,* **65,** 2543–2562.

Thorpe, S. A., 1968: A method of producing a shear flow in a stratified fluid. *J. Fluid Mech.,* **32,** 693–704.

Weinstock, J., 1986: Finite-amplitude gravity waves: Harmonics, advective steepening, and saturation. *J. Atmos. Sci.,* **43,** 688–704.